

June 2007

Multiple-channel silicon micro-resonator based filters for WDM applications

Shijun Xiao

Purdue University

Maroof H. Khan

Birck Nanotechnology Center, Purdue University, mhxan@purdue.edu

Hao Shen

Birck Nanotechnology Center, Purdue University, shen17@purdue.edu

Minghao Qi

Birck Nanotechnology Center, Purdue University, mqi@purdue.edu

Follow this and additional works at: <http://docs.lib.purdue.edu/nanopub>

Xiao, Shijun; Khan, Maroof H.; Shen, Hao; and Qi, Minghao, "Multiple-channel silicon micro-resonator based filters for WDM applications" (2007). *Birck and NCN Publications*. Paper 260.

<http://docs.lib.purdue.edu/nanopub/260>

This document has been made available through Purdue e-Pubs, a service of the Purdue University Libraries. Please contact epubs@purdue.edu for additional information.

Multiple-channel silicon micro-resonator based filters for WDM applications

Shijun Xiao, Maroof H. Khan, Hao Shen and Minghao Qi

Birck Nanotechnology Center, Purdue University, West Lafayette, IN 47907, USA
sxiao@ecn.purdue.edu, mhkhan@purdue.edu, shen17@purdue.edu, mqi@ecn.purdue.edu

Abstract – We demonstrate predictable resonance wavelength shifts in silicon micro-resonators by varying their perimeters using high-resolution lithography. The linear coefficient between the resonance wavelength shifts and the perimeter changes is determined with detailed experiments, and found to be nearly constant across the C and L bands in telecommunications. This empirical coefficient is also compared to that obtained from simulations on straight waveguides. Based on the linear model, without post-fabrication trimming or tuning, an eight-channel wavelength de-multiplexer with reasonably predicted average channel spacing $\sim 1.8 \pm 0.1$ nm (3dB bandwidth $\sim 0.7 \pm 0.1$ nm) is demonstrated at telecommunication bands in a silicon chip for the first time. This filter has out-of-band rejection ratio ~ 40 dB, low channel crosstalk ≤ 30 dB and low channel dropping loss $\leq 4 \pm 1$ dB except for degraded performance in one channel due to fabrication imperfections.

©2007 Optical Society of America

OCIS codes: 250.5300 (photonic integrated circuits); 130.3120 (integrated optical devices); 230.5750 (resonators); 220.4000 (microstructure fabrication)

References and links

1. T. Barwicz, M. A. Popović, M. R. Watts, P. T. Rakich, E. P. Ippen and H. I. Smith, "Fabrication of add-drop filters based on frequency-matched Microring Resonators," *IEEE J. Lightwave Technol.* **24**, 2207-2218 (2006).
2. M. A. Popović, T. Barwicz, M. R. Watts, P. T. Rakich, L. Succi, E. P. Ippen, F. X. Kärtner, and H. I. Smith, "Multistage high-order microring-resonator add-drop filters," *Opt. Lett.* **31**, 2571-2573 (2006).
3. Q. Xu, B. Schmidt, S. Pradhan, and M. Lipson, "Micrometer-scale silicon electro-optic modulator," *Nature* **435**, 325-327 (2005).
4. B. E. Little, J. S. Foresi, G. Steinmeyer, E. R. Thoen, S. T. Chu, H. A. Haus, E. P. Ippen, L. C. Kimerling, and W. Greene, "Ultra-compact Si-SiO₂ microring resonator optical channel dropping filters," *IEEE Photon. Technol. Lett.* **10**, 549-551 (1998).
5. M. S. Nawrocka, T. Liu, X. Wang, and R. R. Panepucci, "Tunable silicon microring resonator with wide free spectral range," *Appl. Phys. Lett.* **89**, 071110 (2006).
6. A. Vörckel, M. Mönster, W. Henschel, P. H. Bolivar, and H. Kurz, "Asymmetrically coupled silicon-on-insulator microring resonators for compact add-drop multiplexers," *IEEE Photon. Technol. Lett.* **15**, 921-923 (2003).
7. P. Dumon, W. Bogaerts, V. Wiaux, J. Wouters, S. Beckx, J. V. Campenhout, D. Taillaert, B. Luyssaert, P. Bienstman, D. V. Thourhout, and R. Baets, "Low loss SOI photonic wires and ring resonators fabricated with deep UV lithography," *IEEE Photon. Technol. Lett.* **16**, 1328-1330 (2004).
8. S. Xiao, M. H. Khan, S. Shen and M. Qi, "Fabrication and characterization of silicon-on-insulator micro-resonators and add-drop filters with free spectral range over 30 nm," submitted, *IEEE J. Lightwave Technol.*
9. S. T. Chu, B. E. Little, W. Pan, T. Kaneko, S. Sato, and Y. Kokubun, "An eight-channel add-drop filter using vertically coupled microring resonators over a cross grid," *IEEE Photon. Technol. Lett.* **11**, 691-693 (1999).
10. C. W. Holzwarth, *et al.* "Accurate resonant frequency spacing of microring filters without postfabrication trimming," *IEEE J. Vac. Sci. Technol. B* **24**, 3244-3247 (2006).
11. Q. Xu, B. Schmidt, J. Shakya, and M. Lipson, "Cascaded silicon micro-ring modulators for WDM optical interconnection," *Opt. Express* **14**, 9431-9435 (2006).
12. Eric Dulkeith, Fengnian Xia, Laurent Schares, William M. J. Green, and Yurii A. Vlasov, "Group index and group velocity dispersion in silicon-on-insulator photonic wires," *Opt. Express* **14**, 3853-3863 (2006)

13. A. C. Turner, C. Manolatou, B. S. Schmidt, and M. Lipson, M. A. Foster, J. E. Sharping, and A. L. Gaeta, "Tailored anomalous group-velocity dispersion in silicon channel waveguides," *Opt. Express* **14**, 4357-4362 (2006)
 14. M. A. Foster, *et al.*, "Broad-band optical parametric gain on a silicon photonic chip," *Nature* **441**, 960-963 (2006).
 15. Y. Vlasov and S. McNab, "Losses in single-mode silicon-on-insulator strip waveguides and bends," *Opt. Express* **12**, 1622-1631 (2004).
 16. B. E. Little, *et al.*, "Very high-order microring resonator filters for WDM applications," *IEEE Photon. Technol. Lett.* **16**, 2263-2265 (2004).
 17. M. S. Rasras, *et al.*, "Tunable narrowband optical filter in CMOS," OFC 2006, PDP 13.
-

1. Introduction

High-index-contrast (HIC) microphotonics is an attractive technology to shrink photonic integrated circuits down to micrometer-scale size, and the miniaturization of filtering devices will significantly reduce the cost of optical communication systems and bring novel applications. HIC waveguides, resonators and filters are fundamental components that have been demonstrated both in silicon nitride (SiN) and in silicon (Si). On the SiN platform, third-order microring filters have been reported for applications in optical add-drop multiplexing (OADM) [1-2]. The reported filtering device is of single channel with a free spectral range of around 20 nm. Compared to SiN, Si has higher index and provides further size reduction and larger tuning range. While silicon resonators and resonator-based filters have been widely reported [3-8], almost all these demonstrations are for a single channel, incompatible with wavelength-division-multiplexing (WDM) applications, where multiple-channel devices are demanded. There have been only a few reports on multiple-channel micro-resonator based filters [9-11]. In reference [9], the reported device was fabricated with low-index-contrast glass material, which is not ideal for dense photonic integrated circuits. In reference [10], the authors reported an eight-channel SiN microring filter bank, where resonance wavelength shifts were achieved via an empirical variation of exposure dose using electron-beam lithography (EBL). The exact amount of dose variations depend on many process conditions, such as the specific lithography tool, resist, device material and substrate. Therefore the dose information can only be obtained in a trial-and-error fashion. Moreover, this is not a technology suitable for high-volume manufacturing as individual control of exposure doses is not supported in high-speed lithography such as optical projection lithography and nano-imprint lithography. In reference [11], the authors reported a four-channel modulator by cascading four silicon microring resonators. However, this reported work was limited to resonators and modulators only, without demonstrations on channel dropping filters.

Here, we report an approach to achieve multiple-channel filters consisting of micro-resonator arrays in silicon, where the individual resonance wavelength of each micro-resonator in the array is shifted by changing its perimeter [9-11]. Although it is known that the resonance wavelength of a micro-resonator can be changed by its perimeter or other geometrical dimensions, to our best knowledge, there has been no systematic study of resonance wavelength shifts over perimeter changes and using it to achieve predictable wavelength shifts, which should be interesting to a wider optics community. In this paper, we derive an analytically linear model where the resonance wavelength shift is proportional to the perimeter change. More importantly, for resonance wavelength shifts ranging from 1 to 7 nm due to different perimeter changes, we experimentally verify this linear model via design, fabrication and characterization of micro-resonators, and the linear coefficient is determined experimentally. This linear model is also compared with parameters obtained from simulation on straight waveguides. Applying the experimentally verified scheme we changed the perimeters of micro-resonators in a uniform step of 80 nm, and demonstrated an eight-channel resonator array in telecommunication bands. We measured responses of eight drop-ports and the through port over the C and L bands (1520-1630 nm). The eight-channel dropping filter has a free spectral range of 16 nm, an average channel spacing of 1.8 ± 0.1 nm, high out-of-band

rejection ratio ~ 40 dB, low channel cross talk ≤ 30 dB and low channel dropping loss $\leq 4\pm 1$ dB in most cases. To the best of our knowledge, this is the first reported work on wavelength de-multiplexer in a silicon chip.

2. Resonance wavelength shift

Race-track shaped resonators (Fig. 1) were chosen for analysis, fabrication and characterization. The reference resonator's perimeter is $P=2\times(L+\pi R)$. The perimeter is varied by adjusting the length of the straight portions of the racetrack from L to $L+\Delta L$, i.e., $\Delta P=2\times\Delta L$, while the bends are kept constant. All waveguides have the same width w . The input/output waveguides, necessary for measuring the response, are placed near the bends and the spacing between the bus and the bend is fixed. This strategy of changing perimeters eliminates several issues, mainly fabrication related, when compared to varying the radius of ring resonators [9-11]. First of all, curved patterns must be broken down or digitized into polygons on a rectangular grid during the pattern generation process, *e.g.*, in electron-beam lithography (EBL). Such digitization errors, around the minimum beam step (2 nm in our case), can be significant when perimeter changes are on the order of 20 nm. A straight waveguide has no digitization error as long as its length and width are multiples of the minimum beam step size in EBL. By keeping the bends fixed, the digitization errors on perimeter change ($\Delta P=2\Delta L$) can be eliminated. Meanwhile, the index distribution in the coupling region is maintained for linear modeling in the following discussions.

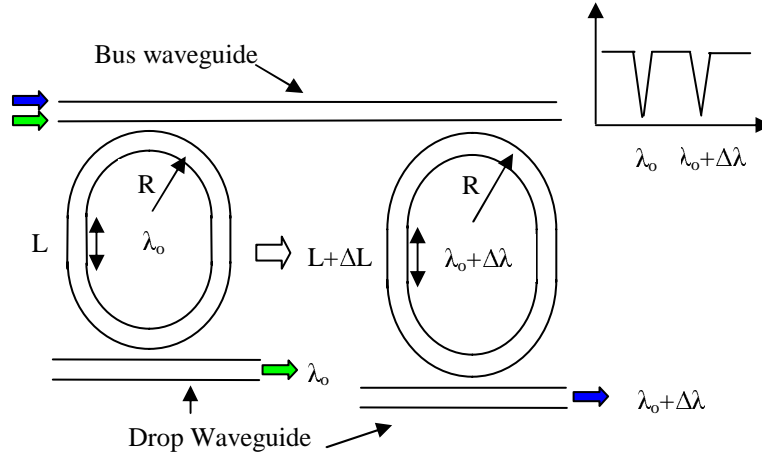


Fig. 1. Theoretical model of changing the resonator's perimeter to shift its resonating wavelength.

As the silicon waveguide has very large dispersion (wavelength dependent index) [12-14], the effective index varies when the resonance wavelength changes. Then, the master equations of resonance for the two resonators shown in Fig. 1 are

$$m\lambda_0 = 2\pi R n_b + 2L n_s \quad (1.a)$$

$$m(\lambda_0 + \Delta \lambda) = 2\pi R(n_b + \Delta n_b) + 2(n_s + \Delta n_s)(L + \Delta L) \quad (1.b)$$

where m is an integer (resonance order), λ_0 is the reference resonating wavelength, n_s is the effective index in the straight waveguide, and n_b is the effective index in the bending waveguide (n_b also includes the coupling induced effective index change). The significant point here is that n_b doesn't change as the resonator's perimeter changes. According to the master equations, the resonance frequency shift $\Delta \lambda$ is

$$\Delta\lambda = \left(\frac{2n_s}{2\pi Rn_b + 2Ln_s} \Delta L \right) / \left(1 - \lambda_o \frac{2\pi R \frac{dn_b}{d\lambda} + 2L \frac{dn_s}{d\lambda}}{2\pi Rn_b + 2Ln_s} - \lambda_o \frac{2 \frac{dn_s}{d\lambda}}{2\pi Rn_b + 2Ln_s} \Delta L \right) \quad (2)$$

where we use $\Delta n_b \approx (dn_b)/(d\lambda) \times \Delta\lambda$ and $\Delta n_e \approx (dn_e)/(d\lambda) \times \Delta\lambda$. Note that $\Delta n_b \approx (dn_b)/(d\lambda) \times \Delta\lambda$ will introduce a larger error in ring-shaped geometry as n_b depends both on the wavelength and bending radius in rings. The racetrack geometry eliminates the n_b dependence on bending radius.

In order to simplify Eq. (2), we need to analyze the effective index in the resonator, i.e., n_b and n_e . The effective index n_b in the bending waveguide is generally difficult to calculate or measure. The effective indices n_s in straight waveguides were calculated with commercial software (Rsoft BPM). As the dispersion in SOI waveguide depends strongly on the exact waveguide dimensions [12-14], we tried two different waveguide widths of 450 nm and 500 nm. The height of 250 nm is determined by SOI wafer (SOITEC). For our waveguide modeling, in addition to the bottom cladding layer of SiO₂, there is another cladding layer (200 nm of hydrogen silsesquioxane, or HSQ) on top of the silicon core, which is used as the etching mask in our fabrication and remains as cladding material. We also use Sellmeier models for wavelength dependent material indices in both silicon and silicon dioxide at room temperature. For wavelengths from 1450 to 1650 nm, at room temperature, the material index decreases monotonically from 3.4846 to 3.4697 in silicon and from 1.4452 to 1.4428 in silicon dioxide (also HSQ). In fact, the material dispersion in silicon dominates that in cladding materials, and the material dispersion in silicon oxide can be ignored while keeping the dispersion in silicon. In our simulation, the wavelength was varied from 1450 nm to 1650 nm with a step of 20 nm, yielding eleven data points of effective indices as a function of wavelength. For each calculated index, the error is estimated to be less than 1%. As the wavelength increases from 1450 nm to 1650 nm, the effective index decreases from 2.517 to 2.240 and from 2.605 to 2.361 for w=450 and w=500 nm respectively. The index n_s is approximately a linear function of the wavelength within this range, thus the first order derivative $(dn_s)/(d\lambda)$ can be viewed as a constant, i.e., $-1.4 \times 10^{-3} \text{ nm}^{-1}$ and $-1.2 \times 10^{-3} \text{ nm}^{-1}$ for widths of 450 nm and 500 nm, respectively. For $\Delta L/(L + \pi R) < 1\%$ in our case, the magnitude of the last term is much smaller than the other two terms in the denominator in Eq. (2). While the exact values of n_b and $(dn_b)/(d\lambda)$ are unknown, it is reasonable to assume that $n_b \approx n_s$ and $(dn_b)/(d\lambda) \approx (dn_s)/(d\lambda)$. Under this assumption, the error of $\Delta\lambda$ is less than around 0.5% (the second term is ~ 1) if the small last term in Eq. (2) is neglected. Thus, we can simplify Eq. (2) to

$$\Delta\lambda = \left(\frac{2n_s}{2\pi Rn_b + 2Ln_s} \Delta L \right) / \left(1 - \lambda_o \frac{2\pi R \frac{dn_b}{d\lambda} + 2L \frac{dn_s}{d\lambda}}{2\pi Rn_b + 2Ln_s} \right) \quad (3)$$

Therefore for small relative perimeter changes in our racetrack configuration, the resonance wavelength shift is proportional to the perimeter change in resonators. This linear model will be verified in our experiment.

If we further assume the effective index in the bending waveguide is equal to that in the straight waveguide, e.g. $n_e = n_b = n_s$ and $(dn_e)/(d\lambda) = (dn_b)/(d\lambda) = (dn_s)/(d\lambda)$, Eq. (3) can be simplified to

$$\Delta\lambda = \left(\lambda_o \frac{\Delta P}{P} \right) / \left(1 - \frac{\lambda_o}{n_e} \times \frac{dn_e}{d\lambda} \right) \quad (4)$$

However, this will result in some non-trivial error and will be discussed in our experiments.

For $\lambda_o = 1550$ nm, $(\lambda_o/n_e) \times (dn_e)/(d\lambda) \approx 1$, and we estimate $\Delta\lambda \approx 0.77 \mu\text{m} \times (\Delta P/P)$. Note that if one neglects the index change with regard to λ , then $\Delta\lambda = 1.55 \mu\text{m} \times (\Delta P/P)$, which is twice larger. For $P = 10\pi \mu\text{m}$ (a ring's perimeter for a radius of $5 \mu\text{m}$), a wavelength shift of $\Delta\lambda = 1$ nm corresponds to a perimeter step ΔP of around 40 nm, which is achievable with state-of-the-art lithography. As the derivative $(dn_e)/(d\lambda)$ is negative, the sign of resonance wavelength shift is the same as the sign of the perimeter shift, e.g., $\Delta P > 0$ corresponding to $\Delta\lambda > 0$, and vice versa. In order to determine the sign of wavelength shift in experiment, in addition to the through response in the bus waveguide, either one of two drop-port responses is needed to determine the resonance wavelength for individual resonator. Thus, the sign of wavelength shift can be determined uniquely in this way. Approximately, to calculate the wavelength shift $\Delta\lambda$ as a function of wavelength, we replace $(dn_e)/(d\lambda)$ with the ratio of finite differences, $(\Delta n_e)/(\Delta\lambda)$, between two immediately adjacent data points. As long as the index varies monotonically and smoothly, which is true in index-guided waveguides, this approximation works well with negligible errors. Therefore,

$$\Delta\lambda_i = \left(\lambda_i \frac{\Delta P}{P} \right) / \left(1 - \frac{\lambda_i}{n_e(i)} \times \frac{n_e(i+1) - n_e(i)}{\lambda_{i+1} - \lambda_i} \right) \quad (5)$$

where, $i = 1, \dots, 10$, and $(\lambda_{i+1} - \lambda_i)$ is 20 nm in our calculation. The theoretical calculation will be compared with experiments in our following discussion.

Two cascaded resonators illustrated in Fig. 1 were fabricated on a silicon-on-insulator (SOI) wafer (from SOITEC). The top silicon layer thickness is 250 nm and the buried oxide is $3 \mu\text{m}$ thick. The device patterns were exposed in a 200 nm-thick hydrogen silsesquioxane (HSQ) with the Vistec (formerly Leica) 100 kV EBL system in the Birck Nanotechnology Center at Purdue University. The beam step is 2 nm and the exposure field size is $0.5 \text{ mm} \times 0.5$ mm. We used inductively-coupled-plasma (ICP) reactive-ion-etch (RIE) with a mixture of Cl_2 and Ar at a pressure of 5 mTorr to etch through the 250 nm silicon layer, using the developed HSQ pattern as etch mask. As the HSQ (spin-on-glass) is of low loss and has a refractive index ~ 1.4 at $1.55 \mu\text{m}$ bands, it is not removed after etch but kept intact as a cladding layer.

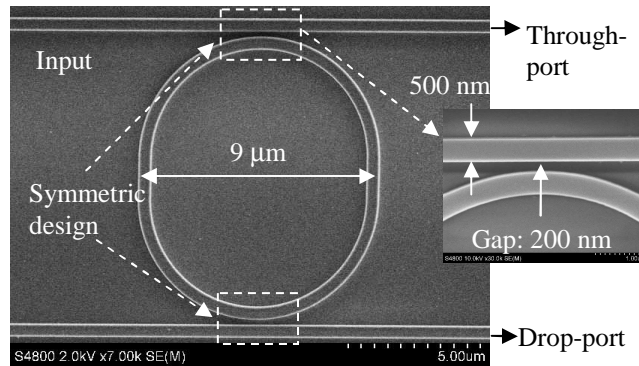


Fig. 2. Scanning-electron-micrograph image of one fabricated micro-resonator channel dropping filter.

Figure 2 is a scanning-electron-microscope (SEM) image showing one of two fabricated cascaded resonators. It has a perimeter of $10\pi \mu\text{m}$ and a constant bend radius of $4.5 \mu\text{m}$. The height h of the silicon core waveguide is 250 nm and the waveguide width w is 500 nm for

both the bus and racetracks. The gaps between racetrack's bends and coupling input/output waveguides are fixed at 200 nm. The fabricated silicon waveguide with cross-section 500 nm×250 nm supports a single mode (TE) for wavelengths from 1.52 μm to 1.63 μm . High-order modes are all cut-off or nearly cut-off with very high losses in waveguides, especially in the bending regions of resonators.

We used an Agilent tunable laser source (wavelengths: 1520 – 1630 nm) to characterize responses of fabricated micro-resonator channel dropping filters. The laser was coupled into the input waveguide through a lensed single mode fiber tip mounted on a XYZ nanopositioning stage. A fiber-based polarization controller was used to rotate the laser polarization to excite the fundamental TE mode of the single mode silicon waveguide. The output was collected by another lensed single mode fiber tip mounted on another XYZ nanopositioning stage and then fed into an optical power meter. The laser wavelength was swept from 1520 nm to 1630 nm at a step of 0.1 nm continuously while the output power of each wavelength was recorded sequentially. Figure 3(a) shows an example of measured responses (power transmission) for two cascaded resonators, where one resonator (closer to the input in layout) has a perimeter of $P = 10\pi \mu\text{m}$, and the other one has a different perimeter of $P = (10\pi - 0.2) \mu\text{m}$. The filter has a free spectral range of around 16 nm. Figure 3(b) is a zoom-in view of the resonance response for these two cascaded resonators, where resonance at two wavelengths $\sim 1538.5 \pm 0.1$ and 1543.5 ± 0.1 nm can be noticed, indicating the expected resonance wavelength shift ~ 5.0 nm, and it is a negative shift ($\Delta\lambda < 0$) compared to the reference resonator. The obvious periodical ripples (≤ 2 dB fluctuation) are due to the Fabry-Pérot effect of the input-output waveguide (~ 5 mm long in our case) used to couple the light into and out of the silicon waveguide. The drop-port response was measured for the resonator with $P = (10\pi - 0.2) \mu\text{m}$, and the obvious notch ~ 10 dB at $\lambda \sim 1543.5$ nm on the drop-port response is due to the reference resonator that is closer to the input in our layout. The drop-port of the reference resonator shows a similar response except a shifted resonance wavelength and without the phenomena of the large notch ~ 10 dB. The -3 dB bandwidth of the drop-port is 0.5 ± 0.1 nm. The measured channel dropping loss is extremely small (≤ 0.5 dB), which indicates a very low intrinsic loss in our fabricated micro-resonator. The intrinsic loss is calculated to be ~ 0.1 dB/round-trip in the resonator, which corresponds to an intrinsic Q over 20,000 in Fig. 3(b). The intrinsic losses in racetrack resonator mainly can be divided into two parts, which are the loss in straight waveguide and the loss in two 180° bends (the bending loss and the mode mismatch loss between the straight waveguide and the bend). The loss in small bends dominates the loss in straight waveguides with comparable or shorter length, and our analysis agrees with previous discussions about the loss in bends with large bending radius $\sim 5 \mu\text{m}$, which is extremely small [15].

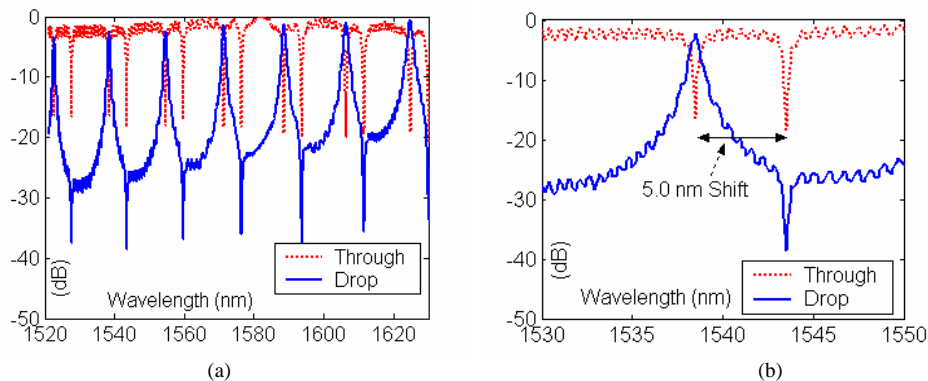


Fig. 3. Measured through-port response (dotted red) and one drop-port's response (solid blue) of a two-channel dropping filter. The drop-port response is normalized to the through-port response. (b) is a zoom-in view of (a). In (b), the two resonances are seen for wavelengths ~ 1538.5 and 1543.5 nm respectively.

We fabricated and tested many sets of two-channel resonators with different perimeter steps. The perimeter of one resonator is kept at $P = 10\pi \mu\text{m}$ for reference while the other was varied from $(10\pi - 0.28) \mu\text{m}$ to $(10\pi + 0.08) \mu\text{m}$. Figure 4 shows resonance wavelength shifts due to perimeter changes for two different reference resonance wavelengths close to 1550 nm. The uncertainty of the experimental wavelength shift is $\pm 0.1 \text{ nm}$ due to the scanned wavelength step. The experimental data can be fitted well with a straight line (the constant term in the linear fitting is very small, well below our data uncertainty), and this is consistent with our theory in Eq. (3). Therefore, we can use $\Delta\lambda = C \times (\Delta P)$ to describe the resonance wavelengths shift, and the coefficient C is a constant that is only related to the geometry of resonators and waveguides. For example, $\Delta\lambda = 0.0225 \times (\Delta P)$ for reference $\lambda_0 \sim 1542 \text{ nm}$, $\Delta\lambda = 0.0227 \times (\Delta P)$ for reference $\lambda_0 \sim 1558 \text{ nm}$, $\Delta\lambda = 0.0228 \times (\Delta P)$ for reference $\lambda_0 \sim 1575 \text{ nm}$, and $\Delta\lambda = 0.0227 \times (\Delta P)$ for reference $\lambda_0 \sim 1592 \text{ nm}$. There is a very small change ($\sim 1\%$ relative change) of the coefficient for reference wavelengths across several free spectral ranges over the C and L bands. Thus the empirical relationship is suitable for predicting resonant wavelength shifts and will be used to design an eight-channel filter.

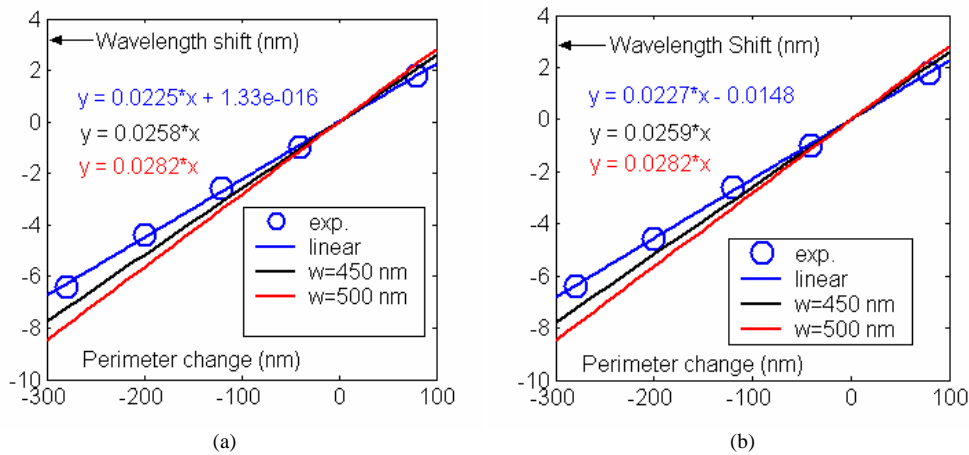


Fig. 4. Resonance wavelength shift vs. perimeter change. (a) is for reference resonance wavelength $\lambda_0 \sim 1542 \text{ nm}$, and (b) is for reference resonance wavelength shift $\lambda_0 \sim 1558 \text{ nm}$. In each plot, a linear fitting is plotted with the experimental data, and the simulated data with Eqs. (4)-(5) is also plotted for comparison.

In Fig. 4, simulated results from Eq. (5) are also plotted for two waveguide widths 450 nm and 500 nm. Compared to simulated resonance wavelength shift at $w=500 \text{ nm}$, the experimentally fitted linear coefficient is 18% smaller. This obvious discrepancy is due to the fact of replacing the effective index (n_b and n_s) in resonators with that in a straight waveguide. To our best knowledge, there is no straightforward way of calculating the effective indices of curved waveguides, n_b and $(dn_b)/(d\lambda)$. Many calculations involve approximations. From Eq. (3), it is possible to extract the values of n_b and $(dn_b)/(d\lambda)$ by fabricating a variety of resonators of different ΔL and $\Delta\lambda$, and compare them with more involved calculations such as cylindrical mode solvers.

3. Eight-channel dropping Filter (wavelength de-multiplexer)

As an important application of our scheme to shift resonance wavelength in micro-resonators, an eight-channel micro-resonator filter (wavelength de-multiplexer) was fabricated and characterized. Figure 5 is an optical image of our fabricated eight-channel filter. We use second-order micro-resonator instead of single one, and a symmetrical design is used. The gap between the bus/drop waveguide and the bend is 200 nm, and the gap between two racetrack's bends is 400 nm. All waveguides are kept at a width of 500 nm. The high-order micro-

resonator yields filtering response with flat passband, fast roll-off and high out-of-band rejection ratio, etc, which are ideal for WDM signal processing [1-2, 8, 16]. On the filter chip, the physical spacing between two adjacent resonators is $100\ \mu\text{m}$ along the input waveguide direction. For a compact design, this spacing can be reduced to $\sim 20\ \mu\text{m}$ so that the core area of a second-order eight-channel filter can be shrunk into a size $\sim 160\times 160\ \mu\text{m}^2$. In Fig. 5, the perimeter of individual resonator in eight second-order resonators is $P+0.32$ (#8), $P+0.24$ (#7), $P+0.16$ (#6), $P+0.08$ (#5), P (#4), $P-0.08$ (#3), $P-0.16$ (#2) and $P-0.24$ (#1) μm , respectively, where $P = 10\pi\ \mu\text{m}$. For the $0.08\ \mu\text{m}$ perimeter step, i.e., $\Delta P = 80\ \text{nm}$, our experimental model $\Delta\lambda = 0.0225 \times (\Delta P)$ predicts a channel spacing of $1.8\ \text{nm}$. Figures 6(a)-6(b) shows the superimposed responses of all eight drop ports normalized to the through port for wavelengths covering C and L bands (1520 to $1630\ \text{nm}$). For a clear view, the full response is divided into two parts that are plotted in Fig. 6(a) for 1526 - $1574\ \text{nm}$ and in Fig. 6(b) for 1574 - $1628\ \text{nm}$ respectively. The black line represents the through-port response. The red and blue lines represent the drop-port responses, whose colors are alternated between two adjacent drop-ports in order to guide the eyes. The wavelength de-multiplexer has a free spectral range around $16\ \text{nm}$, and the filter's response repeats for three times with a period of around $16\ \text{nm}$ in both Fig. 6(a) and Fig. 6(b) as indicated by the horizontal arrowed lines. Within each free spectral range, the channel center wavelength increases as the marked dropping channel number increases, i.e., the passband shifts at an average step of $1.8\pm 0.1\ \text{nm}$ to longer wavelengths from drop-port #1 to drop-port #8.

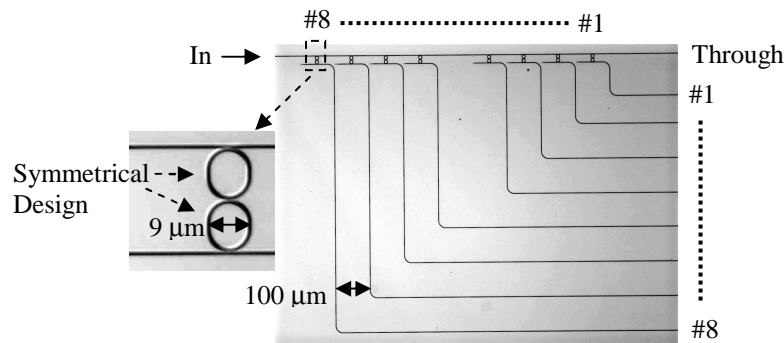
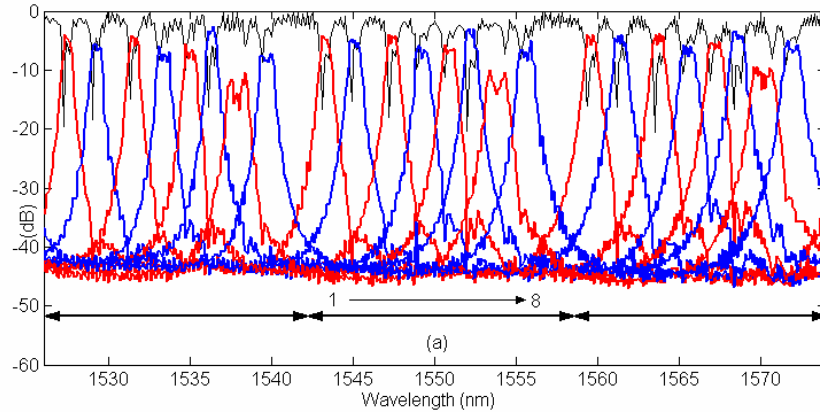


Fig. 5. An optical image of fabricated eight-channel wavelength de-multiplexer



Figs. 6. (a) - 6. (b). Superimposed responses of the through-port (black) and eight drop-ports (red and blue) of the eight-channel dropping filters shown in fig. 5. The horizontal arrowed line indicates a response period around 16 nm. Within one free spectral range, lower channel numbers correspond to shorter channel center wavelengths.

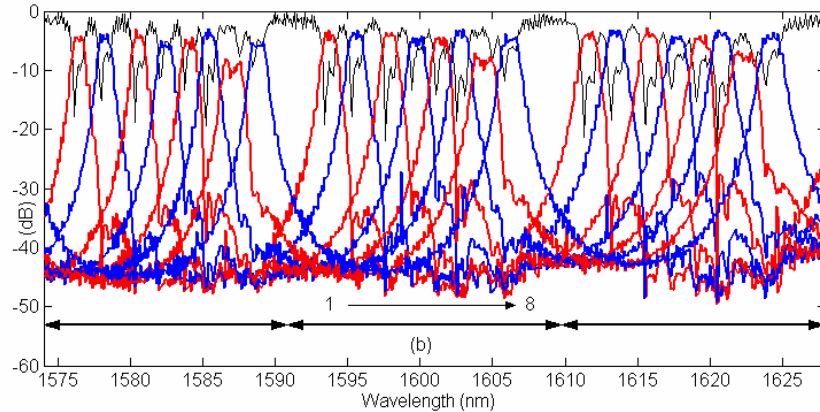


Fig. 6(a)-(b). Superimposed responses of the through-port (black) and eight drop-ports (red and blue) of the eight-channel dropping filters shown in Fig. 5. The horizontal arrowed line indicates a response period around 16 nm. Within one free spectral range, lower channel numbers correspond to shorter channel center wavelengths.

Table 1 Typical channel parameters for the eight dropping channels around ~ 1550 nm.

Channel #	1	2	3	4	5	6	7	8
1dB bandwidth (nm)	0.4	0.5	0.5	0.6	0.7	0.4	1.0	0.7
3dB bandwidth (nm)	0.6	0.7	0.7	1.0	0.9	0.6	1.4	0.9
20dB bandwidth (nm)	1.5	1.8	1.8	2.0	1.8	1.7	2.6	2.2
Center λ (nm)	1543.3	1545.1	1547.4	1549.3	1550.9	1552.2	1553.9	1555.6
Dropping loss (dB)	3.0	3.0	2.0	4.0	4.0	0.5	9.0	4.0
Spacing (nm)	1.8 (1-2)		1.9 (3-4)		1.3 (5-6)		1.8 (7-8)	
	2.3 (2-3)		1.6 (4-5)		1.7 (6-7)			
Isolation (dB)	≤ 30 dB (1-2)		≤ 30 dB (3-4)		≤ 27 dB (5-6)		≤ 20 dB (1-2)	
	≤ 30 dB (2-3)		≤ 25 dB (4-5)		≤ 20 dB (6-7)			
	Non-Adjacent ~ 40 dB limited by the out-of-band rejection ratio							

Table 1 lists the typical parameters related to wavelength de-multiplexing for the eight channels with resonating wavelengths ~ 1550 nm. The bandwidths have an uncertainty of ± 0.1 nm due to the scanned wavelength step, and the drop losses have an uncertainty of ± 1 dB due to Fabry-Pérot ripples on the through-port's response. The ratio between 3dB bandwidth and 20 dB bandwidth is close to 0.5, and this indicates a fast rolling-off response. The obvious degradation of response in channel #7 is due to a large particle sticking to one of the racetracks, which introduces large intrinsic loss and frequency mismatch with regard to the other racetrack. The high dropping loss (9 dB) in channel #7 also results in lower adjacent channel isolation ~ 20 dB. Second-order resonators in all other channels are better matched and have much lower channel dropping loss, narrower channel bandwidth, higher out-of-band rejection ratio ~ 40 dB and higher channel isolation over 30 dB. The average channel spacing is 1.8 nm which is predicted by the experimental model $\Delta\lambda = 0.0225 \times (\Delta P)$. The non-uniform channel spacing is caused by fabrication imperfections over a larger area. Such imperfections are mainly due to electron-beam deflection errors (up to 10 nm according to machine calibration) at the edges and corners of the main deflection field. We believe that these errors can be reduced by shrinking the size of the deflection field and by placing resonators in a region closer to the center of the main deflection field. Alternatively, one can expose each second-order resonator in the same position within a deflection field. Another way to improve device performance is to do post-fabrication trimming or tuning mechanism. For example, the individual resonance frequencies of each micro-resonator in a multi-channel filters could be thermally tuned with micro-heaters [17]. In principle, this integrated silicon de-multiplexer can support 8×40 Gbps high-speed data separation in eight channels.

4. Conclusion

In conclusion, we have demonstrated a linear model where resonance wavelength shift is proportional to perimeter change in micro-resonators, and we derived an analytically linear relation and the linear coefficient is determined with our experiments. Instead of ring resonators, racetrack resonators are adopted for the purposes of eliminating pattern digitization errors and for better linearity in design. The straight section of a racetrack resonator is controlled via precise e-beam lithography to change the resonator's perimeter, and this scheme to shift silicon resonator's resonance wavelength may provide the feasibility of future volume production of multi-channel, micro-resonator based filters. Our scheme should be applicable to multiple-channel resonators design in different material systems. In experiments, we have fabricated and characterized racetrack resonators on a silicon-on-insulator platform. The racetrack resonators have a fixed bending radius of $4.5 \mu\text{m}$ and a perimeter $\sim 10\pi \mu\text{m}$. We show very low channel dropping losses (≤ 0.5 dB) in racetrack resonators, and very low intrinsic losses ~ 0.1 dB/round-trip (not including waveguide coupling losses) is calculated for fabricated silicon racetrack resonators, corresponding to an intrinsic Q over 20,000. Therefore, these racetrack resonators are ideal for high-quality low-loss multiple-channel filters using our scheme to changing the perimeters for resonance wavelength shifting.

As an example of multiple-channel devices for WDM applications, we demonstrated an eight-channel silicon wavelength de-multiplexer with the experimental verified scheme to shift micro-resonator's resonance wavelength. In order to have good passband response for WDM signal processing, we used second-order filters, where each channel consists of two coupled micro-resonator. The eight-channel wavelength de-multiplexer has a free spectral range around 16 nm and an average channel spacing of 1.8 ± 0.1 nm over C and L bands. The average channel spacing matches well with our linear model $\Delta\lambda = 0.0225 \times (\Delta P)$ with trivial errors. For all channels except one, we show low channel crosstalk ≤ 30 dB, low channel dropping loss $\leq 4 \pm 1$ dB with the lowest ~ 0.5 dB. Although further fabrication improvements are needed, our device should be interesting for de-multiplexing eight-channel high-speed data at 40 Gbps in a silicon chip.